Available online at www.sciencedirect.com
SCIENCE DIRECT®
Journal of the Mechanics and Physics of solids
53 (2005) 771–794
JOURNAL OF THE MECHANICS AND PHYSICS OF SOLIDS
www.elsevier.com/locate/jmps

On the stability of Kelvin cell foams under compressive loads

L. Gong[a], S. Kyriakides[a,*], N. Triantafyllidis[b]

[a]*Research Center for Mechanics of Solids, Structures & Materials, The University of Texas at Austin, WRW 110, Austin, TX 78712, USA*
[b]*Department of Aerospace Engineering, Francois-Xavier Bagnoud Building, University of Michigan, Ann Arbor, MI 48109, USA*

Received 15 June 2004; accepted 28 October 2004

Abstract

It has been previously shown that the nonlinearity exhibited in the compressive response of open cell foams is governed by cell ligament buckling. Significant insight into this behavior can be gained by idealizing such foams as periodic, space-filling Kelvin cells assigned several of the geometric characteristics of actual foams. The cells are elongated in the rise direction; the ligaments are assumed to be straight, to have *Plateau* border cross sections, and nonuniform cross sectional area distribution. The mechanical response of such foams can be established using models of a characteristic cell assigned appropriate periodicity conditions. The ligaments are modeled as shear deformable beams. The periodicity of this microstructure allows the use of Bloch wave theory to conduct the search for the critical state efficiently. The method tailored to the present microstructure is outlined. It is subsequently used to establish the critical states for uniaxial and a set of triaxial loadings. A rich variety of buckling modes are identified which are affected by the anisotropy and the mutliaxiality of the applied loads. Under some loadings the critical modes have long wavelengths which are shown to lead to unstable postbuckling behavior involving localization. Under other loading conditions the modes are either local to the characteristic cell or involve an assemblage of a

*Corresponding author. Tel.: +1 512 471 4167; fax: +1 512 471 5500.
E-mail address: skk@mail.utexas.edu (S. Kyriakides).

0022-5096/$ - see front matter
doi:10.1016/j.jmps.2004.10.007

few such cells. For the cases analyzed local modes were found to have a stable postbuckling response.

Keywords: Open-cell foams; Crushing; Stability; Bloch Wave Theory

1. Introduction

Solid foams comprise a class of light-weight cellular materials with exceptional energy absorption characteristics. They are widely used in shock mitigation, in packaging and in cushioning but also as cores in sandwich structures. Cellular materials are abundant in nature but today they are also manufactured out of most man-made materials (polymers, metals, ceramics, carbon, paper) to chosen cell sizes and densities. Their advantageous characteristics are derived from their cellular microstructure. The design of cellular materials requires that the microstructure be related to their properties (mechanical, thermal, acoustic, etc.). Gibson and Ashby's book (1997) gives an excellent review of the state of the art as well as basic information on many types of cellular materials. Hilyard and Cunningham (1994), Weaire and Hutzler (1999) and the book by Ashby et al. (2000) provide articles on a broad range of foam issues from manufacturing to application.

Common to most cellular materials is a compressive stress-displacement ($\sigma - \delta$) response with the characteristic three-regime shape shown in Fig. 1. In regime I the response is stiff and essentially linearly elastic (modulus E^*). This terminates into a limit stress (σ_I) which is followed by an extended stress plateau which comprises regime II (mean stress level $\bar{\sigma}_P$ and extent $\Delta\bar{\varepsilon}_P$). In regime III the response recovers stiffness once more. The limit stress is a sign of the onset of unstable behavior. During the stress plateau, localized deformation bands involving buckled cells initiate and spread throughout the material. The relatively low initial stress peak and

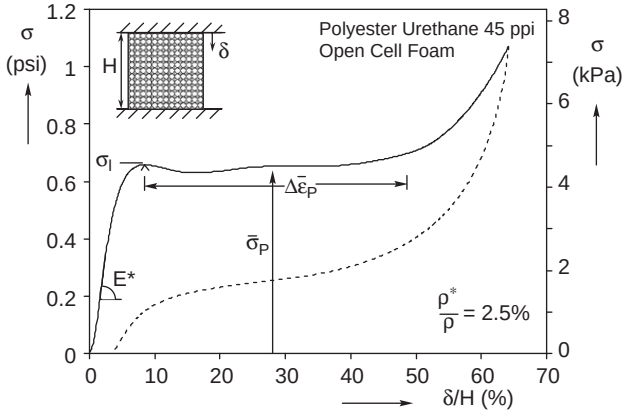

Fig. 1. Compressive stress-displacement response characteristic of many foams.

the extended plateau are defining features of the excellent energy absorption of such materials. (The unloading response is indicated by a dashed line.) Design of cellular materials requires that the deformation history of the microstructure be related to the main variables of this response $\{E^*, \sigma_I, \bar{\sigma}_P, \Delta\bar{\varepsilon}_P\}$. Honeycombs constitute the simpler, two-dimensional version of this class of problems. Papka Kyriakides (1994, 1998a–c) and Triantafyllidis and Schraad (1998) used micromechanics to establish these variables for honeycombs loaded in plane. They demonstrated that instabilities are the root cause of this type of response and that the keys to its successful modeling are first, accurate representation of the geometry of the microstructure and second, measurement and appropriate modeling of the constitutive behavior of the base material.

Gong et al. (2005) and Gong and Kyriakides (2005) have recently applied this general framework to open cell foams. They analyzed polyester urethane foams with nominal cell sizes of 3, 10, 20, 45 and 100 pores per inch (ppi). Their relative densities (ρ^*/ρ) varied between approximately 0.022 and 0.028. The experimental part of the study included: (a) characterization of the cell and ligament morphology; (b) measurement of the mechanical properties of the polymer using ligaments extracted from the foam; and (c) crushing of blocks of foams between rigid parallel plates at various constant displacement rates. The major findings were as follows:

- The microstructure consisted of interconnected polyhedra each with an average of 13.7 faces, each face having an average of nearly 5 sides.
- The size of the cells did not vary significantly.
- The cells were elongated in the rise direction (ratio of diameters in rise-to-lateral directions—λ-ranged from 1.23 to 1.43).
- The ligaments had a three-cusp hypocycloid cross section (*Plateau borders*) and the cross sectional area varied along the length.
- To first order, the microstructure was found to scale with the cell size.
- The base material is an elastomer and, as a result, it is viscoelastic and exhibits Mullin's effect. In this first attempt at the problems, rate dependence was neglected and the material was approximated to be linearly elastic with modulus E and Poisson's ratio v (typical values given in Table 1 of Gong et al. (2005).

Table 1
Fit parameters for corrected relative density power-law relationship (3) for various cross sections

λ	n	k
1	1.7392	0.1803
1.1	1.7426	0.1791
1.2	1.7433	0.1637
1.3	1.7449	0.1580
1.4	1.7474	0.1350
Unif. Xsc	1.8968	0.1395

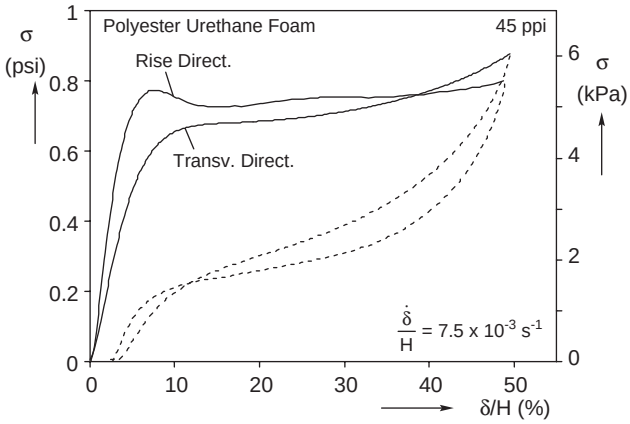

Fig. 2. Comparison of rise and transverse direction compressive responses of a typical open cell foam.

- Because of the anisotropy in the microstructures, the compressive responses in the rise and transverse directions of the foams were different. Fig. 2 shows a comparison of such responses for a 45 ppi foam. The rise direction response exhibits the characteristic three regime behavior described above. It was observed that the blocks tested buckled in an overall manner irrespective of specimen size (Fig. 1, Gong and Kyriakides, 2005). As the stress plateau was traversed, localized deformation involving bands of buckled cells initiated and spread throughout the material. The stress plateau terminates when most of the microstructure has collapsed. The response in the transverse direction has a much smaller elastic modulus but is essentially a monotone. Overall buckling of the test specimens was not observed in this direction.

A sequence of models for predicting all mechanical foam properties of interest has been developed. The foam is idealized to be periodic using the space-filling Kelvin cell (see Fig. 3) assigned several of the geometric characteristics of the actual foams. The cells are elongated in the rise direction; the ligaments are assumed to be straight, to have *Plateau* border cross sections and variable cross sectional area distribution as shown in Fig. 4. An area distribution function developed from measurements has been adopted. The ligaments have been modeled as shear deformable beams.

The first level models are aimed at the initial elastic constants of the anisotropic foam. These have been developed in closed form (Gong et al., 2005) using microsections appropriate for each type loading. The rise and transverse direction moduli predicted for the five foams used in the experiments were found to be in reasonable agreement with the measured values. The second level models are based on the characteristic cell shown in Fig. 5 and are aimed at the initial nonlinear response, the onset of instability and for initial postbuckling studies. The predicted critical stresses and corresponding modes followed the trends seen in the experiments. The third level model is aimed at the large deformation response of

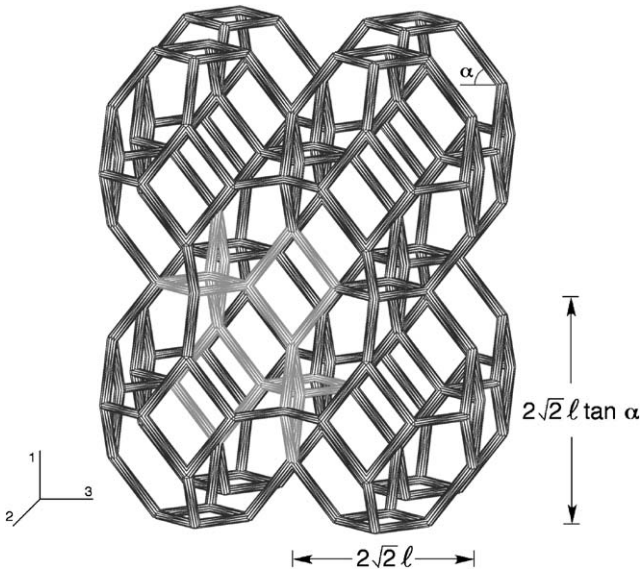

Fig. 3. Cluster of anisotropic Kelvin cells.

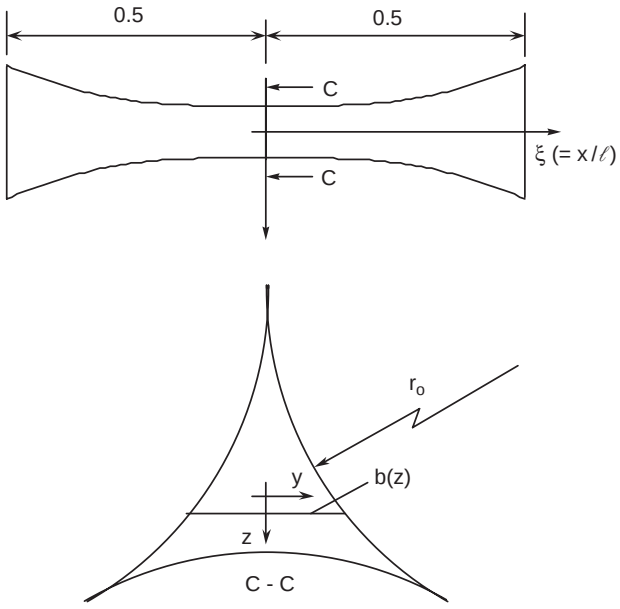

Fig. 4. Geometry of foam ligaments.

the material involving the stress plateau. The localization of deformation and its spreading during the stress plateau are reproduced using large scale, finite size type models involving a large number of cells.

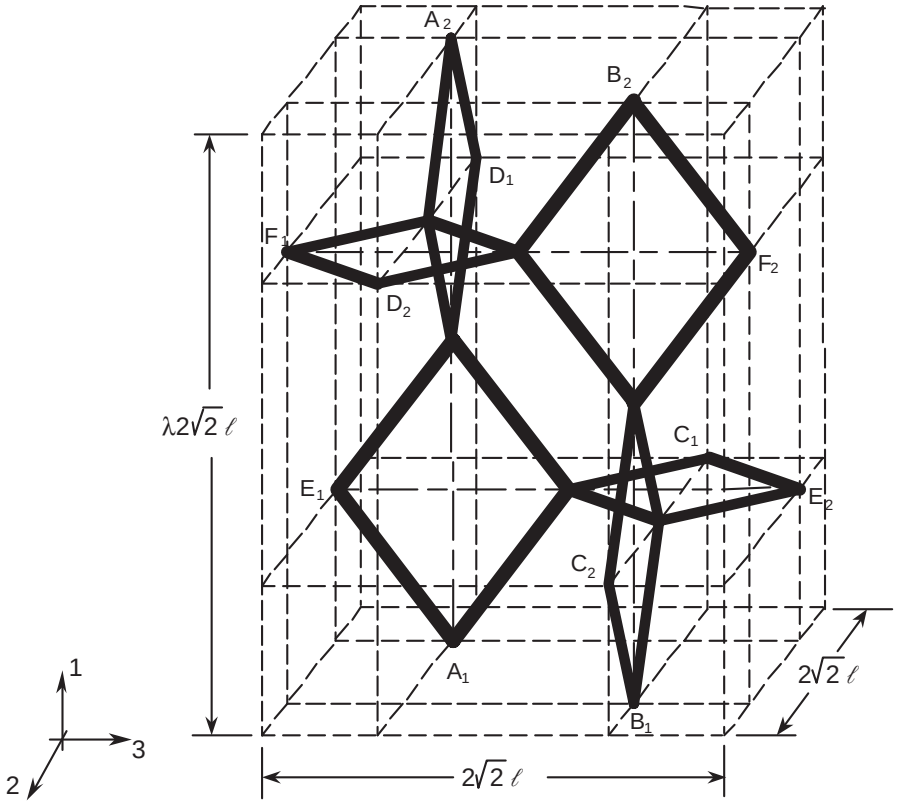

Fig. 5. The Kelvin foam characteristic cell.

An essential requirement of the numerical models is the identification of the critical stress and the associated buckling mode. The complexity of such microstructures, even when idealized, requires that bifurcation checks, involving increasingly larger domains with multiples of the characteristic cell, be made in order to identify the prevalent modes. These include modes local to the cell, others involving several cells and others involving many cells. The corresponding stresses are then compared and the critical stress is identified. Even for just uniaxial compression along the rise and transverse directions considered in Gong and Kyriakides (2005), this process is lengthy. If more general multiaxial loadings are considered the task of establishing a stability surface in an appropriate stress space (say) is daunting.

Because of the periodicity of our microstructure a robust method for establishing the critical conditions under multiaxial loadings based on Bloch waves can make this task more systematic and efficient. In the next section such a method developed by Triantafyllidis and co-workers (Geymonat et al., 1993; Schraad and Triantafyllidis,

1997a,b) will be tailored to the present microstructure. Subsequently, it will be first used to revisit uniaxial loading of the foam and then to generate stability surfaces for a set of triaxial loadings.

2. Analysis

2.1. Anisotropic Kelvin foam and characteristic cell

Most polymeric foams exhibit anisotropy in the form of elongation of the cells in the rise direction. In an effort to mimic this in the Kelvin cell foam, all ligaments with a projection in the x_1-direction are elongated to $\ell/\sqrt{2}\cos\alpha$ ($\alpha \geqslant \pi/4$) while the length of ligaments in the plane normal to x_1 is ℓ. This change makes the height of the cell $h_1 = 2\sqrt{2}\ell\tan\alpha$ and the width $h_2 = 2\sqrt{2}\ell$. An anisotropy parameter λ is defined as

$$\lambda = \frac{h_1}{h_2} = \tan\alpha. \tag{1}$$

The ligaments have a three-cusp hypocycloid cross section shown in Fig. 4 defined by the radius r. The cross sectional area varies along the length (nominal length $= \ell$) according to the empirical relationship

$$A(\xi) = A_0 f(\xi) = A_0(a\xi^4 + b\xi^2 + 1), \quad -0.5 \leqslant \xi = x/\ell \leqslant 0.5 \tag{2}$$

(unless otherwise stated $a = 86$ and $b = 1$ will be used). The sectional properties of the beam are

$$A = \left(\sqrt{3} - \frac{\pi}{2}\right)r^2, \quad I_y = I_z = \frac{1}{24}(20\sqrt{3} - 11\pi)r^4, \quad J = 0.0021r^4 \tag{3}$$

(GJ is an equivalent torsional rigidity which accounts for warping (Warren et al., 1997)). When approximating foam ligaments as beams, a correction is required which involves removal of extra material at the intersection (nodes) of four beams. We adopt the volume correction scheme of Gong et al. (2005) which results in a relative density relationship

$$\frac{\rho^*}{\rho} = k\left(\frac{r_0}{\ell}\right)^n, \tag{4}$$

where k and n depend on the anisotropy variable λ. Table 1 gives values for the constants for specific anisotropy values of interest. (In the absence of this correction $n = 2$, the value most quoted in foam literature.)

A Timoshenko-type correction for the additional deformation resulting from shear stresses will be adopted. The strain energy due to the shear force (V) is modified as follows:

$$U_s = \int_{-1/2}^{1/2} \beta \frac{V^2(\xi)}{2GA}\ell\,\mathrm{d}\xi \quad \text{where } \beta = \frac{A}{I_y^2}\int_z \frac{Q^2(z)}{b(z)}\,\mathrm{d}z. \tag{5}$$

The second integral is over the cross section of the ligament shown in Fig. 4 with Q being the first moment of area about the y-axis ($b(z) \equiv$ width). For this cross section $\beta = 1.24$.

Because of the regularity and periodicity of the microstructure chosen, several of the mechanical properties of interest can be evaluated by considering either the appropriate characteristic cell or an assembly of characteristic cells along with appropriate periodicity conditions. The characteristic cells of the anisotropic Kelvin foam is shown in Fig. 5 (also drawn in color in Fig. 3). The periodicity conditions for a single unit cell can be expressed as follows: Let the three pairs of opposite bounding faces of the cell be $(\partial R_{i1}, \partial R_{i2})$, $i = 1, 2, 3$. The displacements and rotations of points on these faces are, respectively, denoted by (u_{i1}, u_{i2}) and $(\theta_{i1}, \theta_{i2})$, $i = 1, 2, 3$. The following relationships of degrees of freedom are prescribed for points on each pair of faces $(\partial R_{i1}, \partial R_{i2})$ $i = 1, 2, 3$:

$$\begin{aligned} &u_{i1} - u_{i2} = u_{i1}^{\mathrm{ref}} - u_{i2}^{\mathrm{ref}}, \quad i = 1, 2, 3, \\ &\theta_{i1} - \theta_{i2} = 0, \quad i = 1, 2, 3, \end{aligned} \tag{6}$$

where u_{ij}^{ref} $(j = 1, 2)$ are displacements of corresponding points on opposite sides chosen as reference points (e.g., (A_1, A_2), (C_1, C_2), etc.).

The characteristic cell is discretized with finite elements within the nonlinear code ABAQUS using the B32, three-noded, quadratic, space-beam elements. Each ligament is represented by 8 elements of uniform cross-sectional area. The area of each element is based on the symmetric function $f(\xi)$ in (2) as follows:

$$f(\xi) = \begin{cases} 1, & 0 \leqslant |\xi| \leqslant 0.2, \\ 1.482, & 0.2 < |\xi| \leqslant 0.3, \\ 2.574, & 0.3 < |\xi| \leqslant 0.4, \\ 4.993, & 0.4 < |\xi| \leqslant 0.5. \end{cases} \tag{7}$$

By using the *beam general section* feature, the sectional characteristics of each beam $\{A, I_y, J\}$ are prescribed to correspond to the values in (3). The shear correction factor $\beta = 1.24$ is included. The resultant model has 24 ligaments, 192 elements, 378 (951 code) nodes and a total of 2268 variables. As in the preceding work, the foam material is assumed to be linearly elastic with Young's modulus E and Poisson's ratio of 0.49.

2.2. Bloch wave stability calculations

We consider the stability of the infinite periodic foam under general loading following a specified path. We will use the incremental response of the unit cell to this loading, and seek to identify the first instance equilibria different from the trivial one become possible.

Let $\mathbf{K}(\Lambda)$ be the global tangent stiffness matrix of the characteristic cell (unconstrained, i.e. before applying boundary conditions) where Λ is a normalized

load parameter. It can be written as

$$\mathbf{K}(\Lambda) = \begin{bmatrix} \mathbf{K}_{11} & \mathbf{K}_{12} & \mathbf{K}_{1\mathrm{I}} \\ \mathbf{K}_{21} & \mathbf{K}_{22} & \mathbf{K}_{2\mathrm{I}} \\ \mathbf{K}_{\mathrm{I}1} & \mathbf{K}_{\mathrm{I}2} & \mathbf{K}_{\mathrm{II}} \end{bmatrix}, \tag{8}$$

where $\mathbf{K}_{\alpha\beta}$ are stiffness submatrices corresponding to nodes on the three opposite pairs of cell surfaces $(\partial R_{i1}, \partial R_{i2})$, $i = 1, 2, 3$ (subscripts 1 and 2 represent the face pair) and internal nodes are represented by subscript I. So, for example, $\mathbf{K}_{11}$ is a 36×36 matrix for the six nodes $(A_1, B_1), (C_1, D_1), (E_1, F_1)$ on surfaces ∂R_{i1} (see Fig. 5). Each node has 6 degrees of freedom constituting vector $\mathbf{u}_1$ with 36 components. $\mathbf{K}_{22}$ is a similar stiffness matrix corresponding to $(A_2, B_2), (C_2, D_2), (E_2, F_2)$ on surfaces ∂R_{i2} and degrees of freedom $\mathbf{u}_2$ (also with 36 components). $\mathbf{K}_{12}$ and $\mathbf{K}_{21}$ are cross stiffnesses relating $\mathbf{u}_1$ and $\mathbf{u}_2$. $\mathbf{K}_{\mathrm{II}}$ (2196×2196) is the stiffness matrix of the (366) internal nodes with corresponding (2196) degrees of freedom $\mathbf{u}_{\mathrm{I}}$.

Let $\tilde{\mathbf{u}} = \{\tilde{\mathbf{u}}_1, \tilde{\mathbf{u}}_2, \tilde{\mathbf{u}}_{\mathrm{I}}\}^{\mathrm{T}}$ be the displacement increments along a bifurcated equilibrium path starting at the critical point and $\tilde{\mathbf{F}} = \{\tilde{\mathbf{F}}_1, \tilde{\mathbf{F}}_2, \mathbf{0}\}^{\mathrm{T}}$ be the corresponding force increments. Then incremental equilibrium requires that

$$\mathbf{K}(\Lambda)\tilde{\mathbf{u}} = \tilde{\mathbf{F}}. \tag{9}$$

The internal degrees of freedom $\tilde{\mathbf{u}}_{\mathrm{I}}$ can be evaluated from (9) as

$$\tilde{\mathbf{u}}_{\mathrm{I}} = -\mathbf{K}_{\mathrm{II}}^{-1}[\mathbf{K}_{\mathrm{I}1}\tilde{\mathbf{u}}_1 + \mathbf{K}_{\mathrm{I}2}\tilde{\mathbf{u}}_2]. \tag{a}$$

Substituting (a) $\rightarrow$ (9) results in

$$\begin{bmatrix} \hat{\mathbf{K}}_{11} & \hat{\mathbf{K}}_{12} \\ \hat{\mathbf{K}}_{21} & \hat{\mathbf{K}}_{22} \end{bmatrix} \begin{Bmatrix} \tilde{\mathbf{u}}_1 \\ \tilde{\mathbf{u}}_2 \end{Bmatrix} = \begin{Bmatrix} \tilde{\mathbf{F}}_1 \\ \tilde{\mathbf{F}}_2 \end{Bmatrix}, \tag{10}$$

where

$$\begin{aligned} \hat{\mathbf{K}}_{11} &= \mathbf{K}_{11} - \mathbf{K}_{1\mathrm{I}}\mathbf{K}_{\mathrm{II}}^{-1}\mathbf{K}_{\mathrm{I}1}, \\ \hat{\mathbf{K}}_{12} &= \mathbf{K}_{12} - \mathbf{K}_{1\mathrm{I}}\mathbf{K}_{\mathrm{II}}^{-1}\mathbf{K}_{\mathrm{I}2}, \\ \hat{\mathbf{K}}_{21} &= \mathbf{K}_{21} - \mathbf{K}_{2\mathrm{I}}\mathbf{K}_{\mathrm{II}}^{-1}\mathbf{K}_{\mathrm{I}1}, \\ \hat{\mathbf{K}}_{22} &= \mathbf{K}_{22} - \mathbf{K}_{2\mathrm{I}}\mathbf{K}_{\mathrm{II}}^{-1}\mathbf{K}_{\mathrm{I}2}. \end{aligned} \tag{b}$$

Because of the periodicity of the cell we can assume that the bifurcation mode admits the following form (Bloch, 1928)

$$\tilde{\mathbf{u}}(\mathbf{x}) = \mathbf{U}(\mathbf{x}) \exp\left[\mathrm{i}\left(\frac{m_1 x_1}{h_1} + \frac{m_2 x_2}{h_2} + \frac{m_3 x_3}{h_3}\right)\right], \tag{11}$$

where h_i and m_i/h_i, $i = 1, 2, 3$ are the dimensions of the sides of the characteristic cell and the wave numbers, respectively. $\mathbf{U}(\mathbf{x})$ is a periodic function with the same spatial periodicity as the unit cell, i.e.

$$\mathbf{U}(x_1 + n_1 h_1, x_2 + n_2 h_2, x_3 + n_3 h_3) = \mathbf{U}(x_1, x_2, x_3), \tag{c}$$

where n_i are arbitrary integers. In view of (11) nodes on opposite sides will have

$$\tilde{\mathbf{u}}_2 = \boldsymbol{\mu}\tilde{\mathbf{u}}_1 \quad \text{and} \quad \tilde{\mathbf{F}}_2 = -\boldsymbol{\mu}\tilde{\mathbf{F}}_1, \tag{12}$$

where

$$\boldsymbol{\mu} = \begin{bmatrix} e^{im_1}\mathbf{I} & \mathbf{0} & \mathbf{0} \\ \mathbf{0} & e^{im_2}\mathbf{I} & \mathbf{0} \\ \mathbf{0} & \mathbf{0} & e^{im_3}\mathbf{I} \end{bmatrix}, \quad \dim(\mathbf{I}) = 12. \tag{d}$$

Substituting (12) → (10) results in

$$\begin{bmatrix} \hat{\mathbf{K}}_{11} & \hat{\mathbf{K}}_{12} \\ \hat{\mathbf{K}}_{21} & \hat{\mathbf{K}}_{22} \end{bmatrix} \begin{bmatrix} \mathbf{I} & \mathbf{0} \\ \mathbf{0} & \boldsymbol{\mu} \end{bmatrix} \begin{Bmatrix} \tilde{\mathbf{u}}_1 \\ \tilde{\mathbf{u}}_1 \end{Bmatrix} = \begin{bmatrix} \mathbf{I} & \mathbf{0} \\ \mathbf{0} & \boldsymbol{\mu} \end{bmatrix} \begin{Bmatrix} \tilde{\mathbf{F}}_1 \\ -\tilde{\mathbf{F}}_1 \end{Bmatrix}. \tag{13}$$

Multiplying both sides by $[\mathbf{I}\ \ \bar{\boldsymbol{\mu}}]$, where $\bar{\boldsymbol{\mu}}$ is the complex conjugate of $\boldsymbol{\mu}$ (i.e., $\boldsymbol{\mu}\bar{\boldsymbol{\mu}} = \mathbf{I}$), gives

$$[\mathbf{I}\ \ \bar{\boldsymbol{\mu}}] \begin{bmatrix} \hat{\mathbf{K}}_{11} & \hat{\mathbf{K}}_{12} \\ \hat{\mathbf{K}}_{21} & \hat{\mathbf{K}}_{22} \end{bmatrix} \begin{bmatrix} \mathbf{I} & \mathbf{0} \\ \mathbf{0} & \boldsymbol{\mu} \end{bmatrix} \begin{Bmatrix} \tilde{\mathbf{u}}_1 \\ \tilde{\mathbf{u}}_1 \end{Bmatrix} = [\mathbf{I}\ \ \bar{\boldsymbol{\mu}}] \begin{bmatrix} \mathbf{I} & \mathbf{0} \\ \mathbf{0} & \boldsymbol{\mu} \end{bmatrix} \begin{Bmatrix} \tilde{\mathbf{F}}_1 \\ -\tilde{\mathbf{F}}_1 \end{Bmatrix} \tag{e}$$

which results in

$$\overset{\circ}{\mathbf{K}}(\Lambda, \boldsymbol{\mu})\tilde{\mathbf{u}}_1 = [\mathbf{I}\ \ \bar{\boldsymbol{\mu}}] \begin{bmatrix} \hat{\mathbf{K}}_{11} & \hat{\mathbf{K}}_{12} \\ \hat{\mathbf{K}}_{21} & \hat{\mathbf{K}}_{22} \end{bmatrix} \begin{bmatrix} \mathbf{I} \\ \boldsymbol{\mu} \end{bmatrix} \tilde{\mathbf{u}}_1 = [\hat{\mathbf{K}}_{11} + \hat{\mathbf{K}}_{12}\boldsymbol{\mu} + \bar{\boldsymbol{\mu}}\hat{\mathbf{K}}_{21} + \bar{\boldsymbol{\mu}}\hat{\mathbf{K}}_{22}\boldsymbol{\mu}]\tilde{\mathbf{u}}_1 = \mathbf{0}. \tag{14}$$

Here $\overset{\circ}{\mathbf{K}}(\Lambda, m_1, m_2, m_3)$ is a 36×36 Hermitian matrix (i.e., real eigenvalues) with zero determinant. Thus, we prescribe m_i and seek the lowest value of $\Lambda(m_i)$ for which $\det|\overset{\circ}{\mathbf{K}}| = 0$. The process is repeated for a broad range of $m_i \in [0, \pi]$ (note cubic symmetry of cell) and the critical bifurcation load is

$$\Lambda_C = \min_{m_1, m_2, m_3} \Lambda(m_i) \quad \text{at } m_i = m_i^c. \tag{15}$$

The corresponding bifurcation mode is given by

$$\tilde{\mathbf{u}}(\mathbf{x}) = \mathbf{U}(\mathbf{x}) \exp\left[i\left(\frac{m_1^c x_1}{h_1} + \frac{m_2^c x_2}{h_2} + \frac{m_3^c x_3}{h_3} \right) \right]. \tag{16}$$

Two cases are distinguished: either the dimensionless wave numbers at criticality m_i^c are different from 0 (or $2n\pi$) (modes involving a finite number of cells) or they are in the neighborhood of 0. In the latter case two different types of modes coexist; either strictly periodic modes—local to the cell—($m_i^c = 0$, or $2n\pi$) or long wavelength modes ($m_i^c \to 0$). For the strictly periodic modes ($\tilde{\mathbf{u}}_2 = \tilde{\mathbf{u}}_1$) one should be careful to constrain (14) against rigid body translation, thus removing the singularity from $\det|\overset{\circ}{\mathbf{K}}| = 0$. For $m_i^c \to 0$, the limit of $\det|\overset{\circ}{\mathbf{K}}| = 0$ has to be taken analytically and corresponds to the loss of ellipticity of the homogenized tangent moduli of the structure.

To this end, we evaluate the homogenized tangent moduli of the infinite periodic structure under macroscopically uniform unit strains in all possible directions (i.e., three normal and six shear), as follows:

2.2.1. Homogenized moduli of Kelvin cell foam

We construct special functions $\overset{ij}{\boldsymbol{\chi}}$ for the six degrees of freedom of all nodes of the characteristic cell which correspond to unit normal (ε_{ii}, no sum) and shear (ε_{ij}, $i \neq j$) strains as follows:

$$\overset{ij}{\boldsymbol{\chi}} = \left\{ \overset{ij}{\boldsymbol{\chi}}_1, \overset{ij}{\boldsymbol{\chi}}_2, \overset{ij}{\boldsymbol{\chi}}_{\mathrm{I}} \right\}^{\mathrm{T}}, \quad (ij) = 1, 2, 3. \tag{17}$$

For each node (N)

$$\overset{ij}{\boldsymbol{\chi}}(N) = \begin{Bmatrix} \overset{ij}{\boldsymbol{\chi}}_k \\ \overset{ij}{\boldsymbol{\chi}}_r \end{Bmatrix} \quad (k = 1, 2, 3) \quad (r = 4, 5, 6) \tag{f}$$

where subscript k represents the displacements and r the rotations. For the displacement degrees of freedom

$$\overset{ij}{\chi}_k = \delta_{ik} x_j + \overset{ij}{v}_k, \tag{g}$$

where $\mathbf{x}$ are the coordinates of the nodes, $\overset{ij}{v}_k$ are periodic functions

$$\left(\overset{ij}{v}_k \Big|_1 = \overset{ij}{v}_k \Big|_2 \right)$$

and

$$\overset{ij}{\chi}_k \Big|_2 = \overset{ij}{\chi}_k \Big|_1 + \delta_{ik} h_j, \tag{h}$$

where $\bullet|_1$ and $\bullet|_2$ refer to opposite sides of the characteristic cell (the second term on the RHS is only present for surfaces with normals acting in the j-direction). For the rotational degrees of freedom

$$\overset{ij}{\chi}_r \Big|_1 = \overset{ij}{\chi}_r \Big|_2. \tag{i}$$

Applying Eq. (17) to the unit cell, where the internal degrees of freedom are condensed out as in (a), results in

$$\begin{bmatrix} \hat{\mathbf{K}}_{11} & \hat{\mathbf{K}}_{12} \\ \hat{\mathbf{K}}_{21} & \hat{\mathbf{K}}_{22} \end{bmatrix} \begin{Bmatrix} \overset{ij}{\boldsymbol{\chi}}_1 \\ \overset{ij}{\boldsymbol{\chi}}_2 \end{Bmatrix} = \begin{Bmatrix} \overset{ij}{\mathbf{F}}_1 \\ \overset{ij}{\mathbf{F}}_2 \end{Bmatrix}. \tag{j}$$

Using (h), (i) and $\overset{ij}{\mathbf{F}}_2 = -\overset{ij}{\mathbf{F}}_1$ in (j) and multiplying both sides by $[\mathbf{I} \quad \mathbf{I}]$ yields

$$[\mathbf{I} \ \mathbf{I}] \begin{bmatrix} \hat{\mathbf{K}}_{11} & \hat{\mathbf{K}}_{12} \\ \hat{\mathbf{K}}_{21} & \hat{\mathbf{K}}_{22} \end{bmatrix} \begin{Bmatrix} \overset{ij}{\boldsymbol{\chi}}_1 \\ \overset{ij}{\boldsymbol{\chi}}_1 + \langle \delta_{ik} h_j \rangle \end{Bmatrix} = [\mathbf{I} \ \mathbf{I}] \begin{Bmatrix} \overset{ij}{\mathbf{F}}_1 \\ -\overset{ij}{\mathbf{F}}_1 \end{Bmatrix}$$

or

$$[\hat{\mathbf{K}}_{11}+\hat{\mathbf{K}}_{12}+\hat{\mathbf{K}}_{21}+\hat{\mathbf{K}}_{22}]\{\overset{ij}{\boldsymbol{\chi}}_1\}=-[\hat{\mathbf{K}}_{12}+\hat{\mathbf{K}}_{22}]\langle\delta_{ik}h_j\rangle, \tag{k}$$

where $\langle\delta_{ik}h_j\rangle$ are applied to all displacement degrees of freedom of $\overset{ij}{\boldsymbol{\chi}}_1$. This has the solution

$$\overset{ij}{\boldsymbol{\chi}}_1=-[\hat{\mathbf{K}}_{11}+\hat{\mathbf{K}}_{12}+\hat{\mathbf{K}}_{21}+\hat{\mathbf{K}}_{22}]^{-1}[\hat{\mathbf{K}}_{12}+\hat{\mathbf{K}}_{22}]\langle\delta_{ik}h_j\rangle. \tag{18}$$

From $\overset{ij}{\boldsymbol{\chi}}_1$ evaluate $\overset{ij}{\boldsymbol{\chi}}_2$ and $\overset{ij}{\boldsymbol{\chi}}_{\mathrm{I}}$ and form $\overset{ij}{\boldsymbol{\chi}}$.

The incremental moduli of the material at the load Λ can then be evaluated as:

$$L_{ijkl}(\Lambda)=\frac{\overset{ij}{\boldsymbol{\chi}}{}^{\mathrm{T}}\,\mathbf{K}(\Lambda)\,\overset{kl}{\boldsymbol{\chi}}}{V}, \tag{19}$$

where $V=h_1h_2h_3$ is the volume of the unit cell.

Long wavelength instability has been shown (Geymonat et al., 1993) to correspond to the loss of rank one convexity of the above found homogenized moduli of the structure, i.e.

$$(L_{ijkl}(\Lambda)n_jn_l)g_k=0 \quad \text{or} \quad \det|L_{ijkl}(\Lambda)n_jn_l|=0. \tag{20}$$

Define

$$\mathbf{n}=\{\cos\varphi,\sin\varphi\cos\psi,\sin\varphi\sin\psi\}^{\mathrm{T}} \quad 0\leqslant\varphi\leqslant\pi, \quad 0\leqslant\psi\leqslant2\pi. \tag{l}$$

Then for each Λ, vary $\{\varphi,\psi\}$ until (20) is satisfied. The critical load is the lowest Λ which allows such a solution and the corresponding $\mathbf{n}$ is the direction of the band (see also Rice, 1976).

3. Results

3.1. Uniaxial compression in rise direction

Uniaxial compression of one characteristic cell is accomplished by prescribing incrementally the relative displacement (δ_1) between its upper and lower periodic boundaries. Fig. 6a shows the calculated stress-displacement response for a generic anisotropic foam with $\lambda=1.3$ and relative density of 0.025. (For this foam $E_1^*=0.00176E$ can be evaluated from the closed form solution in Table 4 in Gong et al., 2005.) Initially (OAB), the foam deforms uniformly and symmetrically about a vertical axis through the center of the cell (inset shows side view of deformed characteristic cell). The response is stiff but increasingly nonlinear because of the increasingly larger deflections of the ligaments. At some point along OAB an eigenvalue is identified indicating that an alternate equilibrium configuration is possible corresponding to a mode at the cell level. Similar calculations and eigenvalue checks are conducted for columns of N characteristic cells with periodicity conditions at the top, bottom, and sides. For the present microstructure $N=2$ yields the same first eigenvalue and mode, but for $N=3$ the eigenvalue is

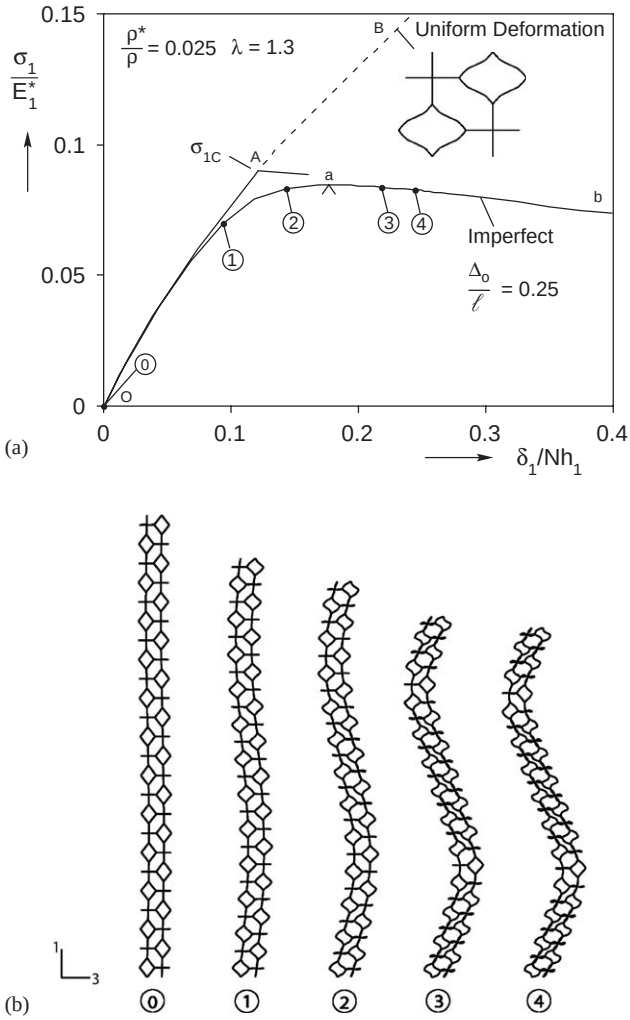

Fig. 6. (a) Calculated prebuckling and postbuckling responses in rise direction, and (b) deformed configurations of periodic column of cells.

smaller. Increasing the number of cells to 4, 6, 8 and 12 reduces further the critical stress and increases the mode wavelength. Fig. 7a illustrates the drop in critical stress with N. For $N>12$ the critical stress remains unchanged although the mode wavelength increases. Similar calculations were performed for wider columns in the x_2-, x_3- and both directions. It was found that widening the column does not affect the critical stress or the corresponding mode.

The Bloch wave method automates the search for the critical state. The method was implemented in conjunction with the code ABAQUS which provided the instantaneous stiffness matrix $\mathbf{K}(\Lambda)$ at different positions along the primary loading

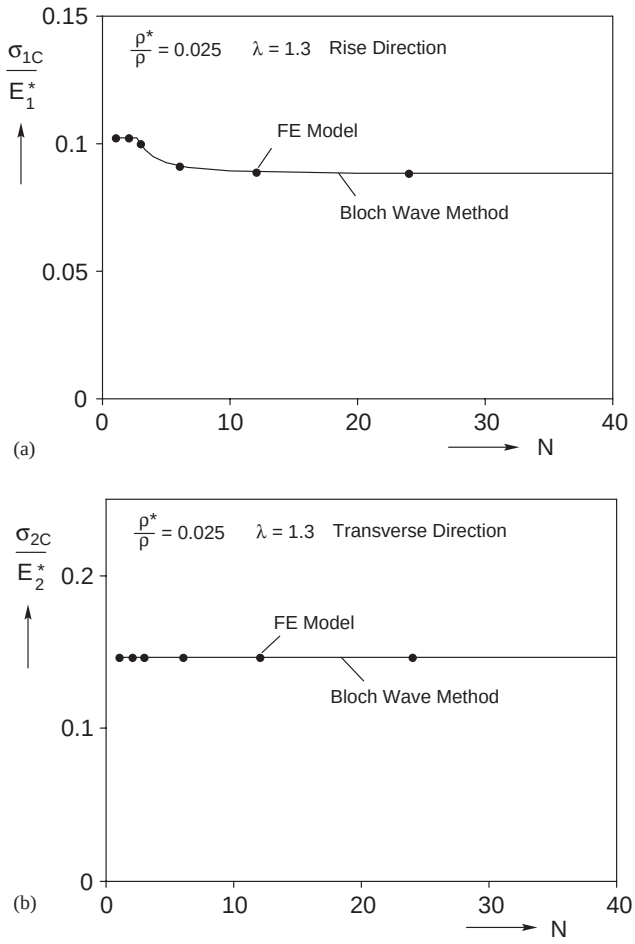

Fig. 7. (a) Critical stress in foam rise direction as a function of number of cells in model analyzed, and (b) critical stress in foam transverse direction as a function of number of cells in model analyzed.

path. At each Λ, m_i $(i = 1, 3)$ are varied from 0 to π and check is made for which values, if any, $\det|\mathbf{K}| = 0$. The critical value of Λ is the lowest value for which this is the case (see Eq. (15)). This search is done by the computer for the stiffness matrices provided by the user for finite increments of Λ. Once buckling is found to occur between two values of Λ, interpolation is used to get close to the critical state.

The results for uniaxial loading in the x_1-direction are drawn with a solid line in Fig. 7a ($N = 2\pi/m$). They are seen to be in agreement with the discrete results obtained via the manual method described above. The critical stress is taken to be the plateau value in Fig. 7a and is identified on the response in Fig. 6a as σ_{1C}. From the results it is evident that the periodic foam admits a long wavelength buckling

mode for this type uniaxial loading. This finding is in concert with the bowing observed in the compressed foam block shown in Fig. 1b in Gong and Kyriakides (2005).

The postbuckling response of the periodic column of cells can be established by adding a small initial geometric imperfection to the domain corresponding to the critical mode ($N = 12$ is selected here). The microsection is then compressed in the x_1-direction by prescribing incrementally δ_1. Results for the case with imperfection amplitude of $\Delta_0/\ell = 0.25$ are included in Fig. 6a ($\Delta_0 = |\boldsymbol{u}_0(\boldsymbol{x})|_\infty$ and $\boldsymbol{u}_0(\boldsymbol{x})$ is the imperfection). The initial and several deformed configurations of a column of cells in the 1–3 plane corresponding to points marked with solid bullets on the response are shown in Fig. 6b. Initially the response follows that of the perfect case. As σ_{1C} is approached, the domain is distorted (see configurations ① and ②) resulting in reduction of its stiffness. With further distortion the response increasingly deviates from that of the perfect case and reaches a limit stress at an average strain of about 17.6%. Subsequently, the stress decreases with deformation. The deformed configurations in Fig. 6b show the progressive growth of the buckled configuration.

The limit stress is imperfection sensitive. The extent of this sensitivity was quantified in Gong and Kyriakides (2005). In addition, they observed that the presence of a limit load instability in the response of this strictly periodic microstructure is a sign that localized deformation patterns may be preferred in a less constrained domain. This was shown to be the case by analyzing finite size domains. Generally both the limit stress and the plateau stress depend on the imperfection amplitude and approach the measured values from above.

3.2. Uniaxial compression in transverse direction

The same process is repeated for uniaxial compression in the transverse direction (x_2). Again we start with one characteristic cell with periodicity conditions on all of its sides and prescribe incrementally the relative displacement (δ_2) between the two sides normal to the x_2-direction. The calculated $\sigma_2 - \delta_2$ response is shown in Fig. 8a. Initially, the deformation involves symmetric crushing of the cell as shown in the inset. The initial modulus is much smaller than the corresponding one in the rise direction ($E_2^* = 0.475E_1^*$). At larger strains the response again becomes increasingly nonlinear due to geometric distortion of the cells. The first eigenvalue occurs at point A at a stress of σ_{2C}.

The domain size is then increased progressively to columns with N characteristic cells. In this direction the critical stress and the corresponding mode were found to be insensitive to N. The critical state was also found to be insensitive to the width of the domain analyzed. These results were also confirmed by the Bloch wave method. Results of σ_{2C} as a function of N predicted by the two methods are compared in Fig. 7b and seen to be in excellent agreement. Thus, the results show that in this direction the prevalent buckling mode is one local to the cell.

The buckling mode corresponding to σ_{2C} with amplitude $\Delta_0 = 0.01\ell$ is now applied as an imperfection to the characteristic cell and the compression test is repeated keeping the same periodicity conditions. The imperfect cell response

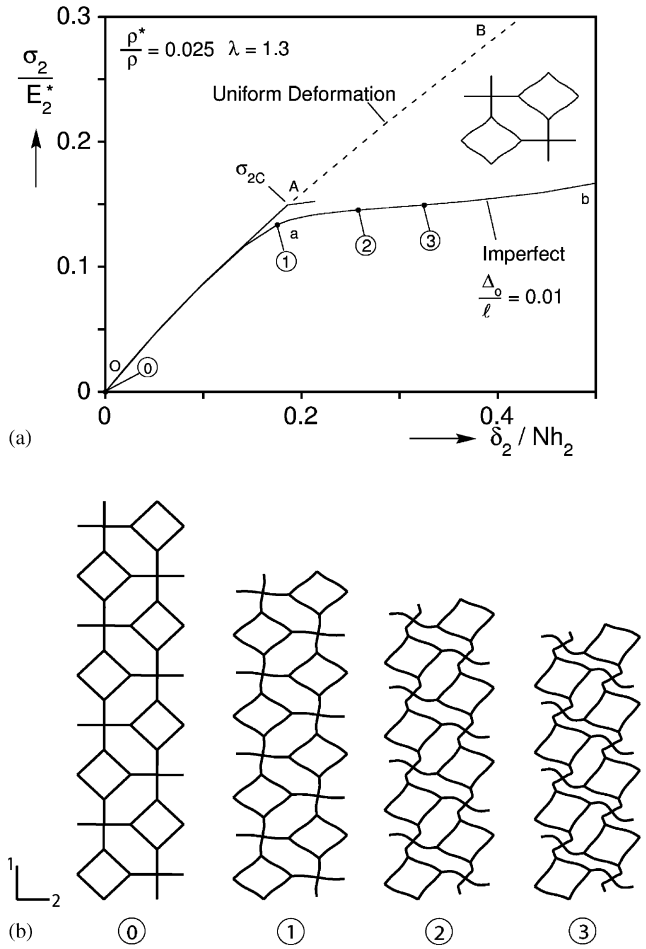

Fig. 8. (a) Calculated prebuckling and postbuckling responses in transverse direction, and (b) deformed configurations showing evolution of local mode.

included in Fig. 8a is seen to initially follow that of the perfect cell. It starts to deviate from it as σ_{2C} is approached. Deformed configurations corresponding to points marked on the response are shown in Fig. 7b. In configuration ① nonsymmetric deformation is visible and it is seen to grow in configurations ② and ③. In contrast to the rise direction, this response maintains a positive slope to large values of average strain. This overall behavior indicates that this deformation pattern will be repeated in larger domains in which the periodicity conditions are relaxed. The monotonic nature of the response is again in agreement with the experimental observations. The "knee" of the response is affected by imperfections as quantified in Gong and Kyriakides (2005).

This dichotomy in behavior between the rise and transverse directions was found to be repeated in Kelvin foams with density ratios less than 6% and anisotropy

values $1<\lambda\leqslant 1.4$. Isotropic foams were found to exhibit the long wavelength unstable buckling mode. For this range of variables the critical stress in the rise direction decreases as the anisotropy increases.

The critical stresses calculated for the five foams tested follow the same trends as the measured limit stresses recorded in the rise direction and the stresses corresponding to the first knee of the transverse direction responses. They are higher than both sets of measurements by about a factor of 2. When imperfections are added to the models the results approach measured values from above.

3.3. Triaxial loading

Porous materials are usually tested under triaxial loading (e.g., Triantafyllou et al., 1989; Deshpande and Fleck, 2000; Gioux et al., 2000). Motivated by this we investigate the stability of our foam under such loading states (Laroussi et al., 2002) used a variation of the Bloch wave method to conduct similar calculations for an isotropic Kelvin cell foam with uniform cross section ligaments; Triantafyllidis and Schraad (1998) used the method to investigate biaxial loading of a honeycomb). Since the material is elastic, surfaces associated with the loss of stability (*failure surfaces*) are independent of the loading path followed. Because of the shape of the failure surfaces traced in the J_2-I_1 plane, we found it convenient to load the foam under the radial stress loading defined by

$$\{\sigma_1,\sigma_2,\sigma_3\}=\Sigma\{k,1,1\}\quad k\in[1,\infty). \tag{21}$$

Thus, $k=1$ represents pure hydrostatic pressure loading and $k\to\infty$ represents uniaxial compression. k was varied and for each value the critical state was established. The Bloch wave method is invaluable in the conduct of such calculations.

Fig. 9a shows the mean stress-change in volume ($\bar{\sigma}-\delta v$) response for hydrostatic compression for a foam with relative density of 0.025 and $\lambda=1.3$ (in this case $\bar{\sigma}=\Sigma$). The mean stress is normalized by the critical stress under uniaxial loading in the rise direction (σ^*_{1C}). The critical stress ($\bar{\sigma}_C$) corresponds to a mode local to a single cell. The postbuckling response was calculated by applying a small initial imperfection to the unit cell corresponding to this buckling mode. The calculated response is shown in the figure while a set of deformed configurations corresponding to the points marked in the response with numbered flags are shown in Fig. 9b (x_1–x_3 and x_2–x_3 planar views are shown). For clarity a $2\times2\times2$ microsection is shown although the repetition of the single cell deformation pattern is quite obvious. Once again the response is a monotone indicating that deformation is stable. Because of the anisotropy most of the deformation occurs in the x_2–x_3 plane where some parts of the microstructure are seen to stay intact whereas the surrounding neighboring ligaments collapse by twisting. The pattern in configuration ③ is reminiscent of patterns seen in the equibiaxial crushing experiments and numerical simulations on circular cell honeycombs of Papka and Kyriakides (1999a, b) (see Figs. I.11 and II.5b). (Note that no ligament contact was applied in these calculations.)

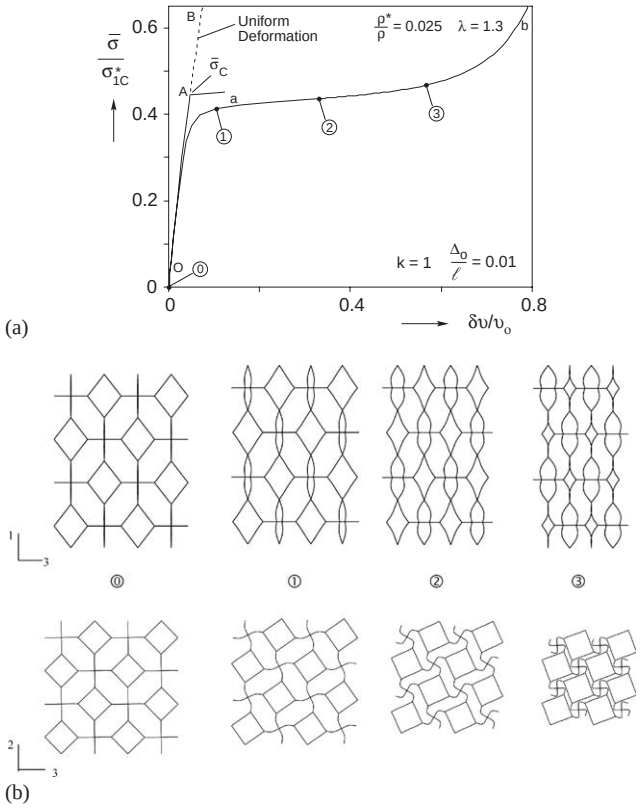

Fig. 9. (a) Calculated prebuckling and postbuckling responses under hydrostatic pressure, and (b) deformed configurations showing evolution of local mode.

Results for a $k = 1.54$ are shown in Fig. 10. Fig. 10a shows the axial stress-displacement response and Fig. 10b the corresponding mean stress-change in volume response (in this case $\bar{\sigma} = \Sigma(2+k)/3$). Both stress quantities are normalized by σ^*_{1C}. The critical state is marked on the responses by σ_{1C} and $\bar{\sigma}_C$. For this loading, the critical buckling mode involves a domain consisting of $2 \times 2 \times 2$ cells. The postbuckling responses corresponding to a small initial imperfection in the form of the critical buckling mode are included in the two figures. Both are monotones indicating that they are stable. However, they exhibit a milder rate of increase than the pure hydrostatic case. Fig. 10c shows two planar views of a sequence of deformed configurations of the $2 \times 2 \times 2$ cell domain analyzed. The evolution of patterns in both domains is quite complex.

Fig. 11a and b show similar responses for $k = 2.5$. In this case the critical state corresponds to a long wavelength mode. Furthermore, the postbuckling responses of the appropriate domain with a small initial imperfection corresponding to this buckling mode exhibit a limit load instability. Fig. 11c shows the initial and three deformed configurations corresponding to the points marked on the responses with

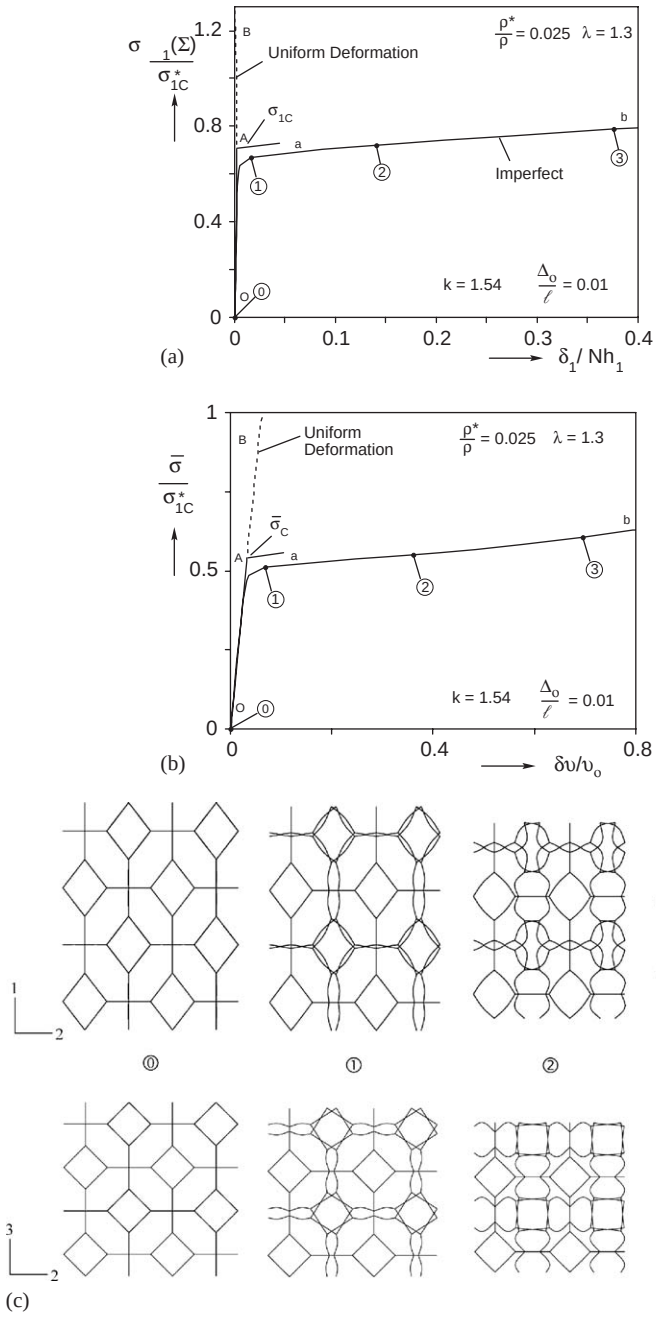

Fig. 10. (a) Calculated axial stress-displacement prebuckling and postbuckling responses for multiaxial load ($k = 1.54$), (b) mean stress-change in volume responses and (c) deformed configurations showing evolution of mode involving $2 \times 2 \times 2$ cell domain.

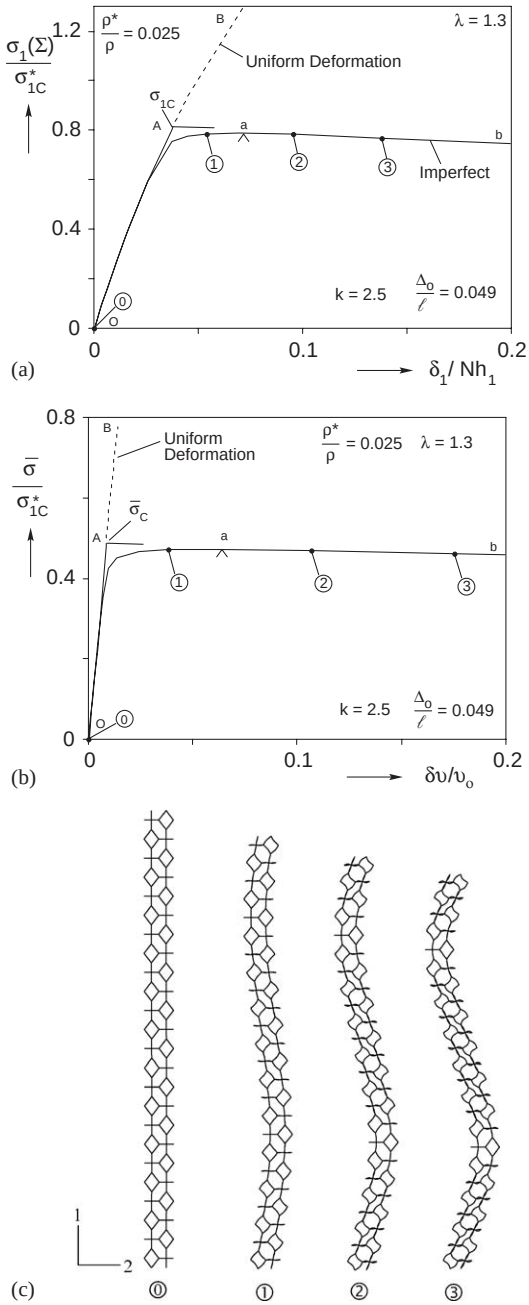

Fig. 11. (a) Calculated axial stress-displacement prebuckling and postbuckling responses for multiaxial load ($k = 2.5$), (b) mean stress-change in volume responses and (c) deformed configurations showing evolution of long wavelength mode.

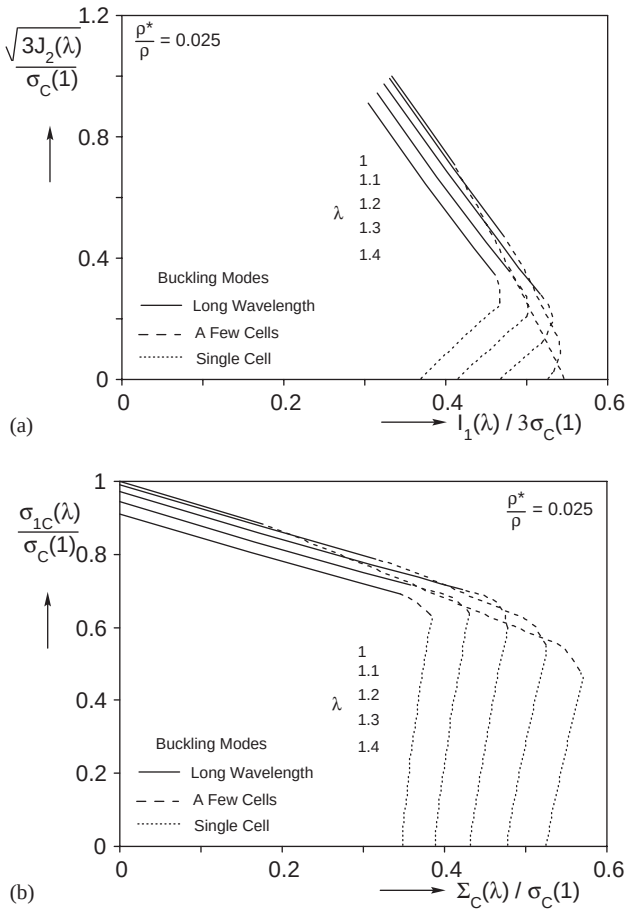

Fig. 12. (a) Anisotropic foam failure envelopes in $\sqrt{3J_2} - I_1$ plane and (b) anisotropic foam failure envelopes in $\sigma_1 - \Sigma$ plane.

numbered flags. The domain analyzed consists of a column of 12 characteristic cells with the usual periodicity conditions applied to the top, bottom and sides. Overall, the behavior is similar to that of the uniaxial loading case shown in Fig. 6. The limit load again implies that if the periodicity conditions are removed deformation will tend to localize.

Additional calculations were conducted for a broad range of k and for each case the critical state was established. The results are summarized in Fig. 12a in the form of a "failure" envelope in the $\sqrt{3J_2} - I_1$ plane (J_2 is the second invariant of the deviatoric stress tensor and I_1 the first invariant of the stress tensor). The two stress quantities are normalized by the critical stress of the same density isotropic foam under uniaxial loading ($\sigma_C(1)$). Interestingly, the shape of the envelope is quite similar to envelopes developed from triaxial tests on aluminum foams by Deshpande

and Fleck (2000). At low values of k (and J_2) the critical mode is local to a single cell. At high values of k (and J_2) the instability involves long wavelength modes. For intermediate values of k (and J_2) the critical buckling modes cover a domain consisting a few cells (e.g. $2 \times 2 \times 2$, $2 \times 2 \times 1$, $1 \times 2 \times 2$, $2 \times 1 \times 2$ cells). In all cases tested the postbuckling responses of long wavelength modes were found to exhibit a limit load. By contrast, local modes exhibit stable postbuckling behavior.

Similar calculations were performed for foams with the same relative density but different values of anisotropy. The results are summarized in Fig. 12a. For all anisotropic cases considered the shapes of the failure surfaces are similar. The isotropic case ($\lambda = 1$) does not exhibit the single cell buckling modes at low values of $k \geqslant 1$. Overall, increasing λ tends to decrease the critical stress states.

An alternate failure envelope is one involving the lateral stress Σ_C vs. the axial stress σ_{1C} (note that here $\{\sigma_2, \sigma_3\} = \{\Sigma, \Sigma\}$). Both are normalized by the critical stress of the isotropic foam with the same density under uniaxial loading ($\sigma_C(1)$). The failure envelopes calculated for five values of anisotropy are shown in Fig. 12b. Because of the different critical states plotted, these envelopes contain additional results not included in Fig. 12a. Again the shapes of the surfaces are qualitatively similar to experimentally produced "yield" surfaces for aluminum foams in Deshpande and Fleck (2000). The isotropic foam essentially encloses all the others. The same three regimes of buckling modes are identified on each envelope.

4. Summary and conclusions

In Gong and Kyriakides (2005) it was demonstrated that the nonlinearity in the compressive response of open cell foams, is governed by cell ligament buckling. Significant insight into this behavior was gained by idealizing such foams as comprising of periodic, space-filling Kelvin cells assigned several of the geometric characteristics of actual foams. The cells were elongated in the rise direction; the ligaments were assumed to be straight, to have *Plateau* border cross sections, and variable cross sectional area distribution. The base material was assumed to be linearly elastic. The modeling involved either a single characteristic cell or an assemblage of several such cells. In all cases appropriate periodicity conditions were prescribed to the domain analyzed.

The complexity of such microstructures requires that bifurcation checks, involving increasingly larger domains with multiples of the characteristic cell, be made in order to identify the prevalent buckling modes. These include modes local to the cell, others involving several cells and others involving many cells. This process can be automated by using Bloch waves to establish the critical states. In this paper a method based on Bloch waves developed by Triantafyllidis and co-workers has been tailored to the present microstructure. The method was then used to find the critical states of such foams under uniaxial and a set of triaxial loadings.

A rich variety of buckling modes were identified which were shown to be affected by the foam anisotropy and the mutliaxiality of the applied loads. For example, for uniaxial compression along the rise direction the critical state is associated with a

long wavelength mode. This mode was shown to exhibit unstable postbuckling behavior leading to localization. By contrast, for uniaxial compression in the transverse direction the prevalent mode is local to the cell. This mode exhibits a stable postbuckling response. Both of these behaviors persisted for all foam anisotropy values considered. It is important to note that both types of the behavior are consistent with experimental observations. Isotropic foams exhibit long wavelength buckling modes.

The response and stability of Kelvin cell foams under triaxial loads was also analyzed. The results were used to develop failure envelopes for foams with varying anisotropy values in the $\sqrt{3J_2} - I_1$ and $\sigma_{1C} - \Sigma_C$ planes. The envelopes corresponding to the isotropic foam were found to enclose (nearly) those of anisotropic foams. For loading states involving relatively small axial stresses (and J_2) in the rise direction, the critical buckling modes were found to be local to the characteristic cell. For loading states involving relatively high axial stresses (and J_2) in the same direction the prevalent buckling modes had long wavelengths. In the transition between the two regimes criticality was associated with buckling modes involving domains of a few cells. For all cases examined, long wavelength modes exhibited unstable postbuckling behavior leading to localization. Modes local to the characteristic cell, or those involving domains of a few cells, were found to have stable postbuckling responses. This richness in buckling modes is a complexity which required the automated bifurcation check procedure provided by the Bloch wave method. More on postbuckling behavior and on localization observed under some loading regimes can be found in Gong and Kyriakides (2005).

Acknowledgements

The work of LG and SK was conducted with financial support from the National Science Foundation through Grant CMS-0245485 and from the Air Force Office of Scientific Research through Grant no. F49620-98-1-0145. The work of NT was supported by the Air Force Office of Scientific Research through Grant no. F49620-99-1-0098. This support is acknowledged with thanks. The authors also wish to thank Foamex International Inc. for providing foam samples and technical support.

References

Ashby, M.F., Evans, A., Fleck, N.A., Gibson, L.J., Hutchinson, J.W., Wadley, H.N.G., 2000. Metal Foams: A Design Guide. Butterworth-Heinemann, Oxford.

Deshpande, V.S., Fleck, N.A., 2000. Isotropic constitutive models for metallic foams. J. Mech. Phys. Solids 48, 1252–1283.

Gibson, L.J., Ashby, M.F., 1997. Cellular Solids: Structure and Properties, second ed. Cambridge University Press, Cambridge.

Gioux, G., McCormac, T.M., Gibson, L.J., 2000. Failure of aluminum foams under multiaxial loads. Int. J. Mech. Sci. 42, 1097–1117.

Geymonat, G., Müller, S., Triantafyllidis, N., 1993. Homogenization of nonlinearly elastic materials, microscopic bifurcation and macroscopic loss of rank-one convexity. Arch. Rat. Mech. Anal. 122, 231–290.

Gong, L., Kyriakides, S., 2005. Compressive response of open-cell foams. Part II: Initiation and spreading of crushing. Int. J. Solids Struct., 42, 1381–1399.

Gong, L., Kyriakides, S., Jang, W.-Y., 2005. Compressive response of open-cell foams. Part I: Morphology and elastic properties. Int. J. Solids Struct., 42, 1355–1379.

Hilyard, N.C., Cunningham, A. (Eds.), 1994. Low Density Cellular Plastics: Physical Basis of Behavior. Chapman & Hall, London.

Laroussi, M., Sab, K., Alaoui, A., 2002. Foam mechanics: nonlinear response of an elastic 3D-periodic microstructure. Int. J. Solids Struct. 39, 3599–3623.

Papka, S.D., Kyriakides, S., 1994. In-plane compressive response and crushing of honeycomb. J. Mech. Phys. Solids 42, 1499–1532.

Papka, S.D., Kyriakides, S., 1998a. In-plane crushing of a polycarbonate honeycomb. Int. J. Solids Struct. 35, 239–267.

Papka, S.D., Kyriakides, S., 1998b. Experiments and full-scale numerical simulations of in-plane crushing of a honeycomb. Acta Mater. 46, 2765–2776.

Papka, S.D., Kyriakides, S., 1998c. In-plane crushing of a polycarbonate honeycomb. In: de Borst, R., van der Giessen, E. (Eds.), Proceedings of the IUTAM Symposium Material Instabilities in Solids, June 1997, Delft. Wiley, Chichester, England, pp. 159–183.

Papka, S.D., Kyriakides, S., 1999a. In-plane biaxial crushing of honeycombs: Part I Experiments. Int. J. Solids Struct. 36, 4367–4396.

Papka, S.D., Kyriakides, S., 1999b. In-plane biaxial crushing of honeycombs: Part II Analysis. Int. J. Solids Struct. 36, 4397–4423.

Rice, J.R., 1976. The localization of plastic deformation. In: Koiter, W.T. (Ed.), Proceedings of the ICTAM 1976, Delft. North-Holland Publishing Co, Amsterdam, pp. 207–220.

Schraad, M.W., Triantafyllidis, N., 1997a. Scale effects in media with periodic and nearly periodic microstructures. Part I: Macroscopic properties. ASME J. Appl. Mech. 64, 751–762.

Schraad, M.W., Triantafyllidis, N., 1997b. Scale effects in media with periodic and nearly periodic microstructures. Part II: Failure mechanisms. ASME J. Appl. Mech. 64, 763–771.

Triantafyllidis, N., Schraad, M.W., 1998. Onset of failure in aluminum honeycombs under general in-plane loading. J. Mech. Phys. Solids 46, 1089–1124.

Triantafyllou, T.C., Zhang, J., Shercliff, T.L., Gibson, L.J., Ashby, M.F., 1989. Failure surfaces for cellular materials under multiaxial loads-II. Comparison of models with experiment. Int. J. Mech. Sci. 31, 665–678.

Warren, W.E., Nielsen, M.K., Kraynik, A.M., 1997. Torsional rigidity of a Plateau border. Mech. Res. Commun. 24, 667–672.

Weaire, D., Hutzler, S., 1999. The Physics of Foams. Oxford University Press, Oxford.